Dispersion Versus Diffusion in Mixing Fronts

Gauthier Rousseau, Satoshi Izumoto, Tanguy Le Borgne, Joris Heyman

AGU ADVANCING EARTH AND SPACE SCIENCES

Water Resources Research

RESEARCH ARTICLE
10.1029/2023WR035848

Dispersion Versus Diffusion in Mixing Fronts

Gauthier Rousseau[1,2], Satoshi Izumoto[1], Tanguy Le Borgne[1], and Joris Heyman[1]

[1]Univ. Rennes 1, CNRS, Géosciences Renne, Rennes, France, [2]Institute of Hydraulic Engineering and Water Resources Management, Vienna, Austria

Abstract Mixing fronts form when fluids with different chemical compositions are brought into contact. They influence a large range of biogeochemical processes in hydrological systems. An important mechanism governing mixing rates in such fronts is stretching by non-uniform flows that accelerates diffusive mass transfer by enhancing concentration gradients. In a range of systems, including porous media at Darcy scale, hydrodynamic dispersion dominates over diffusion to control local mixing rates. As it differs from diffusion through its velocity-dependent dispersion tensor, it is not known how local dispersion interacts with macroscopic mixing front stretching. Here, we investigate the impact of local dispersion versus diffusion on the properties of steady mixing fronts created by both uniform and non-uniform flows. We derive analytical solutions for the concentration profile, mixing scale and mixing rate across the fronts. We validate these predictions by comparison with numerical simulations and experiments performed in quasi two-dimensional tanks over a broad range of Péclet numbers. Without porous media, the mixing scale is governed by local diffusion coupled with flow: it increases diffusively along streamlines in uniform flows while it is constant in converging flows due to the balance between fluid compression and local diffusion. With porous media, the Batchelor scale is no longer sustained and the mixing scale grows with dispersion in non-uniform flows. In addition, the coupling between flow acceleration and dispersion results in a flow rate independent mixing interface, in contrast with the local diffusion scenario. We discuss the consequences of these findings on mixing rates in mixing fronts.

Plain Language Summary This study explores mixing in fluids with and without the presence of a dispersive matrix such as porous media. It highlights the difference of mixing rates in miscible solutes interfaces in the presence or absence of hydrodynamic dispersion, in uniform and non-uniform flow fields. We find that the mixing scales and mixing rates in the presence of dispersion media follows different laws than their well-known diffusive counterparts. These findings provide new insights into mixing and reaction processes controlling a range of applications, such as contaminant transport and remediation, water quality, and subsurface energy storage and extraction.

Gauthier Rousseau and Satoshi Izumoto contributed equally to this work

Key Points:

- The effect of diffusive versus local dispersion on mixing front dynamics is studied under uniform and non-uniform flows
- Analytical solutions for the mixing width and flux are derived for all scenarios and validated through simulations and experiments
- While diffusion and local dispersion produce similar mixing front dynamics in uniform flows, they fundamentally differ in non-uniform flows

Correspondence to:

J. Heyman,
joris.heyman@univ-rennes.fr

Citation:

Rousseau, G., Izumoto, S., Le Borgne, T., & Heyman, J. (2023). Dispersion versus diffusion in mixing fronts. *Water Resources Research*, *59*, e2023WR035848. https://doi.org/10.1029/2023WR035848

Received 26 JUL 2023
Accepted 20 OCT 2023

Author Contributions:

Conceptualization: Gauthier Rousseau, Satoshi Izumoto, Tanguy Le Borgne, Joris Heyman
Data curation: Gauthier Rousseau, Satoshi Izumoto
Formal analysis: Gauthier Rousseau, Satoshi Izumoto
Funding acquisition: Tanguy Le Borgne, Joris Heyman
Investigation: Gauthier Rousseau, Satoshi Izumoto, Tanguy Le Borgne, Joris Heyman
Methodology: Gauthier Rousseau, Satoshi Izumoto

1. Introduction

Mixing fronts formed by miscible fluids influence a range of hydrological and biogeochemical processes (Dentz et al., 2011; Rolle & Le Borgne, 2019; Valocchi et al., 2019) including river-groundwater exchanges (Bandopadhyay et al., 2018; Hester et al., 2017; Ziliotto et al., 2021), freshwater-saltwater mixing in coastal areas (Abarca et al., 2007; De Vriendt, 2021), subsurface microbial processes (Bochet et al., 2020) and mixing in river confluences and estuaries (Bouchez et al., 2010; Prandle, 2009; Yuan et al., 2022). They are also present in many engineering applications, such as soil and groundwater remediation (Fu et al., 2014; Karadimitriou & Hassanizadeh, 2012; Wang et al., 2022), geological carbon sequestration (Szulczewski et al., 2012; Zoback & Gorelick, 2012), hydrogen storage (Lysyy et al., 2022; Tarkowski, 2019) and geothermal systems (Burté et al., 2019). The heterogeneity of flow fields at various scales leads to stretching of mixing fronts, leading to the enhancement of concentration gradients and the resulting mixing rates (Chiogna et al., 2012; Cirpka et al., 2011, 2015; De Barros et al., 2012; Dentz et al., 2023; Engdahl et al., 2014; Le Borgne et al., 2014; Rolle & Le Borgne, 2019; Rolle et al., 2009; Villermaux, 2019; Ye et al., 2015, 2020). The interplay between fluid stretching and diffusion has been captured by lamellar models, that represent mixing fronts as stretched elementary lamellae (in 2D) or sheets (in 3D), in porous media (Heyman et al., 2020; Le Borgne et al., 2013, 2015; Souzy et al., 2020) and turbulent flows (Villermaux, 2019). While this approach has successfully described the coupling between stretching and diffusion, it does not account for situations where dispersion dominates locally over diffusion. This occurs in a range of hydrological systems, including porous media at Darcy scale (Dentz et al., 2011).

Project Administration: Tanguy Le Borgne, Joris Heyman
Resources: Gauthier Rousseau, Satoshi Izumoto
Software: Gauthier Rousseau, Satoshi Izumoto
Supervision: Tanguy Le Borgne, Joris Heyman
Validation: Gauthier Rousseau, Satoshi Izumoto
Visualization: Gauthier Rousseau, Satoshi Izumoto
Writing – original draft: Gauthier Rousseau, Satoshi Izumoto, Tanguy Le Borgne, Joris Heyman
Writing – review & editing: Gauthier Rousseau, Satoshi Izumoto, Tanguy Le Borgne, Joris Heyman

Hydrodynamic dispersion is driven by the combination of molecular diffusion and pore-scale flow variability (Bear, 1988). It is classically modeled as an anisotropic effective dispersion coefficient, whose magnitude is proportional to flow velocity (Delgado, 2007), as opposed to constant diffusion coefficients. Such velocity dependent local dispersion is disregarded in studies that use Hele-Shaw cells as experimental analogs of porous media to study mixing fronts, density driven flows, and reactions (De Wit, 2020). The velocity dependence of the dispersion coefficient has been shown to play an important effect on mixing rates at the salt-fresh water interfaces in porous media (De Vriendt et al., 2022) and in Poiseuille flows (Perez et al., 2019). However, it is not generally known how to quantify its effect on mixing front properties under non-uniform flows.

Here, we investigate the role of dispersion versus diffusion on mixing front properties under both uniform and non-uniform flows. As a paradigm of non-uniform flow, we consider a mixing front created by the convergence of opposing flows. Such flow leads to the appearance of a stagnation point (a point of null velocity) and frequently arise in hydrological systems (Bresciani et al., 2019). This includes hyporheic zones where groundwater upwelling locally competes with flow recirculation produced by variations in the river bathymetry (Hester et al., 2017), fresh-salt water interfaces (De Vriendt, 2021), density-driven flows (Hidalgo et al., 2015). The velocity field close to a stagnation point is non-uniform, with a constant velocity gradient magnitude close to the stagnation point. This means that the flow is constantly decelerating/accelerating when approaching/departing from the stagnation point. This leads to a net stretching of fluid elements and a constant compression rate of mixing fronts. Under the assumption of local diffusion, such compression is known to sustain chemical gradients over a fixed characterize length scale called the Batchelor scale (Villermaux, 2019). While the coupling between stretching and diffusion is well understood is such flows, it is not known how these dynamics are altered by local dispersion.

The paper is organized as follows. In the first section, we solve analytically the steady advection-dispersion equation governing a conservative mixing interface under a constant compression rate. We obtain analytical predictions for the concentration profile, the mixing scale and the mixing rate across the interface. We validate these predictions by comparison with numerical simulation of the coupled flow-dispersion problem. In the second section, we compare these predictions to tank experiments of conservative tracer in uniform and non-uniform flows. We investigate mixing fronts both in the presence and absence of porous media, which lead to respectively local diffusion and local dispersion.

2. Theory

2.1. Mixing Under Advection Diffusion/Dispersion

We consider the transport of a conservative solute in a two-dimensional incompressible flow field with velocity $\boldsymbol{u}(x, y)$, following:

$$\frac{\partial c}{\partial t} = -\boldsymbol{u}(x, y) \cdot \nabla c(x, y) + \nabla \cdot (\boldsymbol{D}(x, y) \cdot \nabla c(x, y)), \tag{1}$$

where $\boldsymbol{D}$ is the dispersion tensor.

To compare the effect of diffusion and dispersion, we consider two models: (a) a constant diffusion coefficient, $\boldsymbol{D}(x, y) = D\boldsymbol{I}$ or (b) a velocity dependent dispersion coefficient (Bear, 1988):

$$\boldsymbol{D} = (D_m + \alpha_T |\boldsymbol{u}|)\boldsymbol{I} + (\alpha_L - \alpha_T)\frac{(\boldsymbol{u} \otimes \boldsymbol{u})}{|\boldsymbol{u}|} \tag{2}$$

where $|\boldsymbol{u}|$ denotes the norm of the velocity vector, $\otimes$ is the outer product, $\boldsymbol{I}$ is the identity matrix and D_{m} the effective molecular diffusion in porous media. α_T and α_L are the transverse and longitudinal dispersivities. Equation 2 implies that the dispersion coefficients parallel and transverse to the local flow direction are respectively

$$D_{\mathrm{L}} = D_{\mathrm{m}} + \alpha_L |\boldsymbol{u}|. \tag{3}$$

and

$$D_{\mathrm{T}} = D_{\mathrm{m}} + \alpha_T |\boldsymbol{u}|. \tag{4}$$

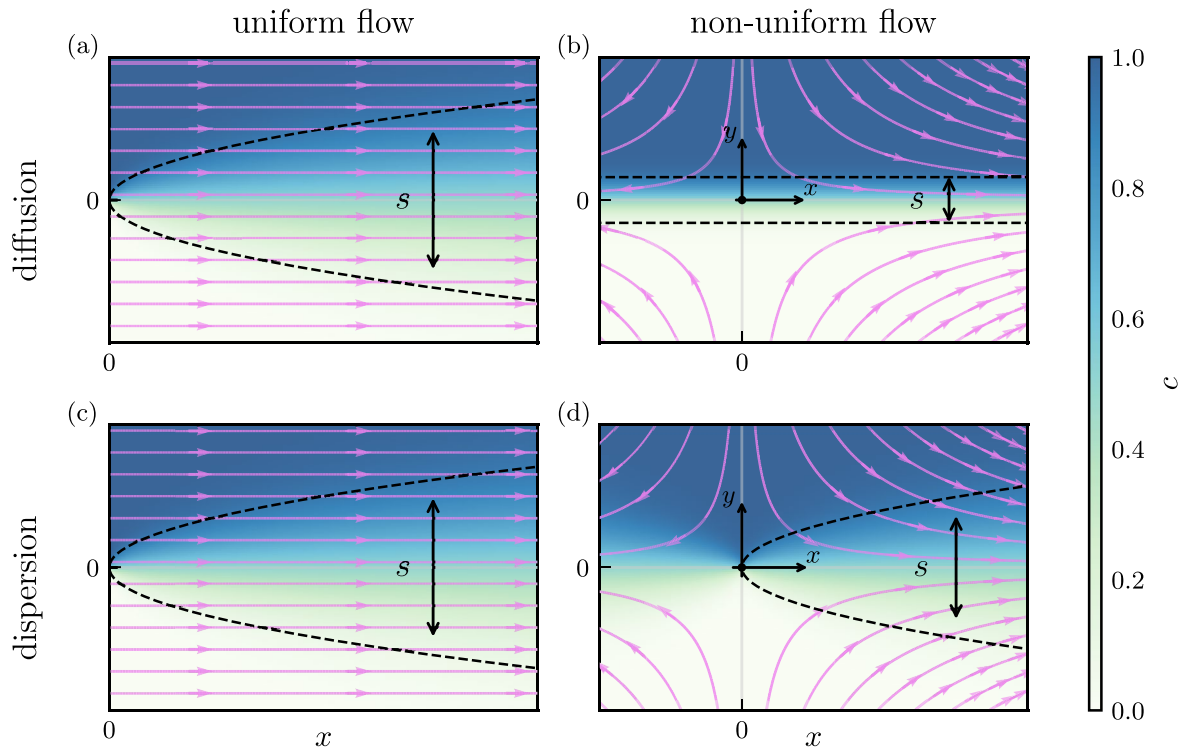

Figure 1. Numerical simulations showing the mixing interface of a conservative solute c in a uniform (left column) and non-uniform flow (right column), if dispersion is assumed constant (top) or proportional to the velocity (bottom). The dotted lines show the extent of mixing width given by theory (Equation 9 for a and c, $s_B = \sqrt{2D/\gamma}$ for b and Equation 22 for d.).

To highlight the difference produced between these two models in mixing front properties, we consider a uniform and a non-uniform flow field.

2.2. Uniform Flow

First, we consider the trivial case of a uniform flow with constant velocity U (Figure 1a) where

$$\boldsymbol{u}(x, y) = \begin{bmatrix} U \\ 0 \end{bmatrix}. \tag{5}$$

Since the flow velocity is constant, dispersion is also a constant tensor $\boldsymbol{D}$ and the transport equation is

$$\frac{\partial c}{\partial t} = -\boldsymbol{u} \cdot \nabla c + \boldsymbol{D}\Delta c \tag{6}$$

We impose the boundary condition to be a continuous solute injection at the flow inlet on the half plane ($c(x = 0, y > 0) = 1$), a so-called co-flow configuration (Figure 1a). Continuous time-independent injection leads to the existence of a steady-state solution of the mixing interface, so that $\partial c/\partial t = 0$. As illustrated in Figures 1a and 1c, concentration gradients are much larger along y than along x directions, and mixing occurs mostly through transverse diffusion/dispersion. Hence, Equation 6 can be approximated by:

$$U\frac{\partial c}{\partial x} = D_{\mathrm{T}}\frac{\partial^2 c}{\partial y^2} \tag{7}$$

whose solution is

Table 1
Theoretical Mixing Width s and Rate J Dependence With Problem Quantities for the Uniform and Non-Flow and in Diffusive and Dispersive Conditions

	Uniform flow	Non-uniform flow
Mixing width s		
diffusive	$s = 2\sqrt{\frac{D_m x}{U}}$	$s \sim \sqrt{\frac{2D_m}{\gamma}}$
dispersive	$s \sim 2\sqrt{\alpha_T x}$	$s \sim 2\sqrt{\frac{\alpha_T x}{3}}$
Mixing rate J		
diffusive	$J \sim \sqrt{\frac{D_m U}{4\pi x}}$	$J \sim \sqrt{\frac{D_m \gamma}{2\pi}}$
dispersive	$J \sim U\sqrt{\frac{\alpha_T}{4\pi x}}$	$J \sim \gamma\sqrt{\frac{3\alpha_T x}{4\pi}}$

Note. For Dispersive, Results are Given in the Limit $\alpha_T U \gg D_m$.

$$c(x, y) = 1/2\left[1 + \mathrm{erf}\left(\frac{y}{s(x)}\right)\right] \tag{8}$$

where erf is the error function. The mixing width $s(x)$ is:

$$s = 2\sqrt{\frac{D_\mathrm{T}}{U}x}. \tag{9}$$

The characteristic concentration gradient and mixing flux along the interface are respectively,

$$\nabla c(x) = \frac{1}{\sqrt{\pi}}\frac{1}{s} = \frac{1}{2\sqrt{\pi}}\sqrt{\frac{U}{D_\mathrm{T}x}} \tag{10}$$

and

$$J(x, y = 0) = D_\mathrm{T}\nabla c = \frac{1}{2\sqrt{\pi}}\sqrt{\frac{U D_\mathrm{T}}{x}} \tag{11}$$

The mixing front properties for diffusion and dispersion dominated regimes are thus obtained by substituting D_T from Equation 4 in the equations above. The results are synthesized in table 1.

2.3. Non-Uniform Flow

We now focus on the case of a non-uniform flow characterized by a constant stretching/compression rate γ induced by converging flows (Figure 1b). This flow represents a paradigm of stretching enhanced mixing (Izumoto et al., 2022; Rolle & Le Borgne, 2019; Villermaux, 2019). Linearization of the flow field around the stagnation point leads to the velocity field

$$\boldsymbol{u}(x, y) = \begin{bmatrix} \gamma & 0 \\ 0 & -\gamma \end{bmatrix}\begin{bmatrix} x \\ y \end{bmatrix} + o\left(x^2, y^2, xy\right), \tag{12}$$

where $\gamma = \partial \boldsymbol{u}/\partial x|_{0,0}$. This velocity field imparts a constant compression rate γ^{-1} to fluid elements in the y direction, and a constant stretching rate γ in the x-direction. Compression acts at enhancing scalar gradients in the y direction, with a direct impact on solute transport and mixing as discussed below.

2.3.1. Diffusion in Non-Uniform Flow

We first consider a constant diffusion coefficient isotropic in the flow domain $\boldsymbol{D} = D_\mathrm{m}\boldsymbol{I}$. Since the compression rate is constant, this system is locally equivalent to chaotic flows where constant compression/stretching rates are sustained globally due to exponential elongation rates (Batchelor et al., 1959; Heyman et al., 2020; Lester et al., 2013, 2016; Villermaux, 2019). The balance of compression rate of fluid elements $\frac{1}{s}\frac{ds}{dt} = -\gamma$ and the rate of diffusive expansion $\frac{1}{s}\frac{ds}{dt} = \frac{2D_\mathrm{m}}{s^2}$ leads to the emergence of a fixed mixing scale

$$s_B \sim \sqrt{\frac{2D_\mathrm{m}}{\gamma}}. \tag{13}$$

This scale, at which solute gradients are maintained, is called the Batchelor scale (Batchelor et al., 1959; Villermaux, 2019). The concentration profile across the mixing interface is obtained by solving Equation 1 with the linearized flow field (Equation 12). The boundary conditions consist of continuous injection of solute on one side of the stagnation point, for example, $c(x, y = \infty) = 1$ and $c(x, y = -\infty) = 0$. The solute c is advected and mixes transversally along the mixing interface located on the x-axis (Figure 1b). Concentration gradients along x are null because both the y component of the velocity and the boundary conditions are independent of x. As before, the continuous injection of solute leads to a steady-state mixing interface, govern by:

$$-y\frac{\partial c}{\partial y} = \frac{D_\mathrm{m}}{\gamma}\frac{\partial^2 c}{\partial y^2}. \tag{14}$$

The solution of this equation is an error function,

$$c(x, y) = 1/2\left[1 + \mathrm{erf}\left(\frac{y}{s_B}\right)\right] \tag{15}$$

with a constant mixing width given by the Batchelor scale $s = s_B$. The characteristic concentration gradient and mixing flux per unit area of the interface are respectively,

$$\nabla c(x) = \frac{1}{\sqrt{\pi}}\frac{1}{s_B} = \frac{1}{\sqrt{2\pi}}\sqrt{\frac{\gamma}{D_\mathrm{m}}} \tag{16}$$

and

$$J(x, y = 0) = D_\mathrm{m}\nabla c = \sqrt{\frac{D_\mathrm{m}\gamma}{2\pi}} \tag{17}$$

We synthesize the results in Table 1.

2.3.2. Dispersion in Non-Uniform Flow

We now consider a dispersion coefficient proportional to flow velocity in non-uniform flow, thus varying in space. We impose the same boundary conditions as before and assume that the mixing interface remains close to the position $y = 0$, where the flow velocity is almost parallel to the x direction ($|\boldsymbol{u}| \sim \gamma x$). Within such approximation, Equation 1 for stationary flows $\left(\frac{\partial c}{\partial t} = 0\right)$ simplifies to

$$0 = \gamma\, y\frac{\partial c}{\partial y} - \gamma\, x\frac{\partial c}{\partial x} - \frac{\partial}{\partial y}\left((D_m + \alpha_T\gamma\, x)\frac{\partial c}{\partial y}\right) + \frac{\partial}{\partial x}\left((D_m + \alpha_L\gamma\, x)\frac{\partial c}{\partial x}\right). \tag{18}$$

We define dimensionless variables $(X, Y) = (x/L_x, y/L_y)$, with L_x and L_y being the characteristic length of observation in the x and y directions, respectively. We focus on the solution near the mixing front and away from the stagnation point, where $y/x = L_y/L_x = \delta_L \ll 1$. In this domain, we can neglect the contribution of molecular diffusion ($\alpha_T\gamma x \gg D_m$). We observe that the relative change in the mixing width is small along the length L_x and get $(\partial c/\partial x)/(\partial c/\partial y) \sim L_y/L_x \ll 1$. Equation 18 then gives

$$-\delta_L^2\, Y\frac{\partial c}{\partial Y} + \delta_L^2\, X\frac{\partial c}{\partial X} = \frac{\alpha_T}{L_x}\frac{\partial}{\partial Y}\left(X\frac{\partial c}{\partial Y}\right) + \frac{\alpha_L}{L_x}\delta_L^2\frac{\partial}{\partial X}\left(X\frac{\partial c}{\partial X}\right). \tag{19}$$

We finally consider that L_x is much larger than the grain size d and, consequently, the dispersion coefficient α_T and α_L ($\alpha_T/L_x \ll 1$ and $\alpha_L/L_x \ll 1$). Keeping only the leading order terms, we can neglect the longitudinal dispersive term in the right-hand side of the equation. Thus, Equation 18 simplifies to

$$-y\frac{\partial c}{\partial y} + x\frac{\partial c}{\partial x} = \frac{\partial}{\partial y}\left(\alpha_T\, x\frac{\partial c}{\partial y}\right). \tag{20}$$

The concentration profile is found by assuming the functional form $c(y) = A\,\mathrm{erf}\left(\frac{y}{\sqrt{K\alpha_T x}}\right) + B$. $K = 4/3$ is determined so that the equation satisfies Equation 20, and boundary conditions. Thus, the solution is,

$$c(y) = 1/2\left[1 + \mathrm{erf}\left(\frac{y}{\sqrt{4/3\alpha_T x}}\right)\right] \tag{21}$$

This leads to a mixing width,

$$s = 2\sqrt{\frac{\alpha_T x}{3}}. \tag{22}$$

The characteristic concentration gradient and mixing flux per unit area of the interface are respectively,

$$\nabla c(x) = \frac{1}{\sqrt{\pi}}\frac{1}{s} \sim \frac{1}{\sqrt{\pi}}\sqrt{\frac{3}{4\alpha_T x}} \tag{23}$$

and

$$J(x, y = 0) = \frac{\alpha_T \gamma x}{\sqrt{\pi}} \nabla c \sim \frac{\gamma}{\sqrt{\pi}} \sqrt{\frac{3\alpha_T x}{4}} \tag{24}$$

We validated the analytical solution for the mixing width Equation 22 and for the flux Equation 24 by numerical simulations of the full advection-dispersion equation using the OpenFOAM code (Figure 1 and Appendix A). Thus, the mixing front and flux properties are similar as for uniform flows, although the mixing width is reduced by a factor $1/\sqrt{3}$ and the normalized flux is increased by a factor of $\sqrt{3}$. We summarize the theoretical dependence of the mixing width and mixing rate with space in Table 1.

3. Experiments

In the following, we test the theoretical predictions against conservative tracer experiments in quasi-two dimensional cells in the presence and absence of porous media.

3.1. Experimental Setup

Two cells with parallel flat plates were designed to achieve (a) uniform flow and (b) non-uniform flow created by converging flows. The thickness of the cells was chosen to be small compared to the longitudinal and transverse dimensions. The uniform flow cell is a rectangular cell with a co-injection of tracers at the inlet (Figure 2a). The co-injection of two solutions produces a mixing interface that propagate toward the outlet at the other side of the cell (Figure 2a). The non-uniform flow cell is designed with four branches of hyperbolic shape with $y = \pm a/x$, a being a constant, that reproduces the geometry of streamlines near a stagnation point created by opposing flows (Equation 12). Flow inlets and outlets are facing each other (Figure 2b), creating a stagnation point and an horizontal mixing interface in the middle cell.

Two sets of conservative transport experiments were performed in these parallel flat plates cells, with and without porous media. We use the empty cell as a reference for mixing in the presence of diffusion with parallel flat plates distanced by small gap ($w = 2$ mm) thus assuring an Hele-Shaw flow condition. The diffusive Hele-Shaw experiments are presented in terms of the Péclet number calculated as $\mathrm{Pe} = w\ U/D_m$. The experiments with porous media were carried out in thicker cells (12 mm) to have a sufficient number of grain diameters in the cell thickness to represent a Darcy scale set up. In this case, we use the porous media Péclet number as $\mathrm{Pe} = d\ U/D_m$ where U and d are respectively a characteristic velocity and grain size. As porous material, we used Fluorinated Ethylene Propylene (FEP 100 X, Chemours©) grains of mean grain diameter 2 mm. This material has the advantage of being transparent in water and have a refractive index ($n = 1.34$) very close to that of water ($n = 1.33$), limiting light scattering (see Appendix B for details) (Amini & Hassan, 2012). These optical properties allow quantifying the depth integrated mixing width of the interface. The porosity of the packed FEP was measured to be 0.37. This is determined by calculating the volume of packed FEP beads based on the packed weight and the density of the FEP.

3.2. Experimental Protocol

First, the cells are filled with deionized water. To fully saturate the media, we first injected CO_2 gas, which dissolved into the injected water hence preventing the presence of bubbles. The cells are placed on top of a blue LED panel to measure solute concentration by fluorescence. The mixing interface is produced by injecting clear and fluorescein tracer solutions at the same rate by a syringe pump. When the mixing front has stabilized, we image the interface with a digital camera (Sony A7s, F2.8/90) equipped with a green band pass filter (Midopt BN532). The image resolution was 0.04 mm per pixel in all experiments. Before each experimental run, we take two images of the cell fully filled with (a) pure water (image intensity I_0) and (b) the fluorescein solution (image intensity $I_{\max}$). The signal emitted by the fluorescein could be approximated as linear with the concentration in this range of concentration. This was done by injecting 6 fluorescein solutions with increasing concentrations into the flow cell packed with FEP, and compare their fluorescence signal to their concentration (see in Annex C a calibration curve). Finally, a normalized tracer concentration is then computed with $c = (I - I_0)/(I_{\max} - I_0)$, with I the raw image intensity. Thus, c varies between 0 and 1. The signal emitted by the fluorescein exhibited

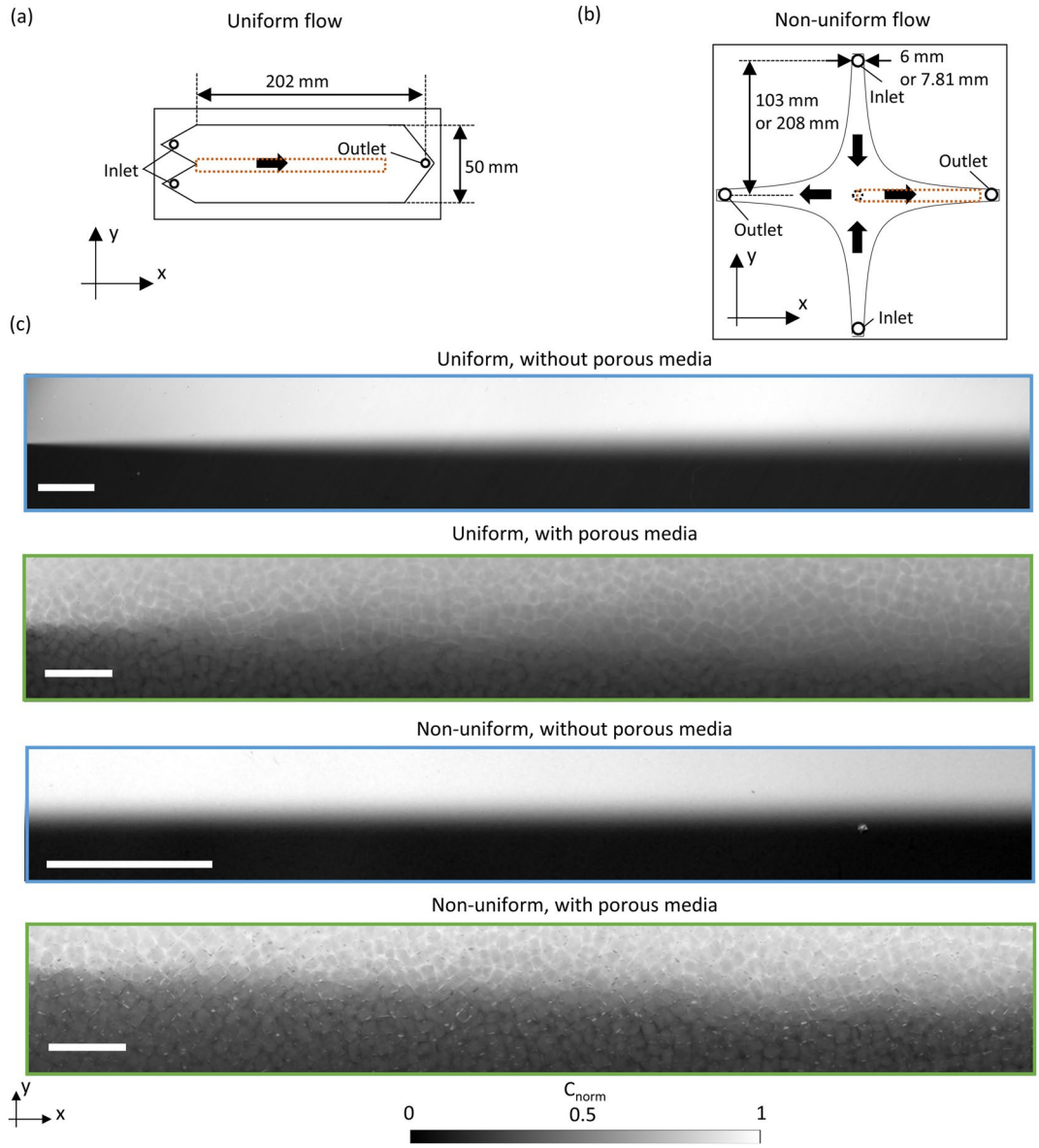

Figure 2. (a, b) Experimental design of (a) the uniform flow cell and (b) non-uniform flow cell. The brown dotted lines indicate the flow regions shown in (c). The thickness of cell is 2 mm for the Hele-Shaw cell (without porous media) and 12 mm with porous media. The non-uniform cell has a length of 103 mm ($a = 303$ mm^2) without porous media and 208 mm with porous media ($a = 811$ mm^2). The thick arrows indicate the direction of the flow. (c) Tracer concentration field in uniform flow (top two rows) and non-uniform flow cases (bottom two rows). Flow is from left to right. The white bars represent 10 mm.

linearity within this concentration range. To confirm this, we introduced six fluorescein solutions with increasing concentrations into the FEP-packed flow cell and compared their fluorescence signals with their respective concentrations (refer to Annex C for the calibration curve). We calculated a normalized tracer concentration, denoted as c, using the formula $c = (I - I_0)/(I_{max} - I_0)$, where I represents the raw image intensity. Thus, c ranges between 0 and 1.

Each experiment was performed for 9 flow rates, corresponding to 9 Péclet numbers. The molecular diffusion coefficient of the fluorescein sodium salt is 4.2×10^{-10} m^2 s^{-1} (Casalini et al., 2011). In the non-uniform flow cell, the characteristic length scale of the velocity gradient γ is estimated from the distance between the injection and the stagnation point $L_c = 10$ cm for the setup without porous media. The compression rate is estimated by v_{inj}/L, with v_{inj} the velocity at the injection and L the distance between the injection and the stagnation point.

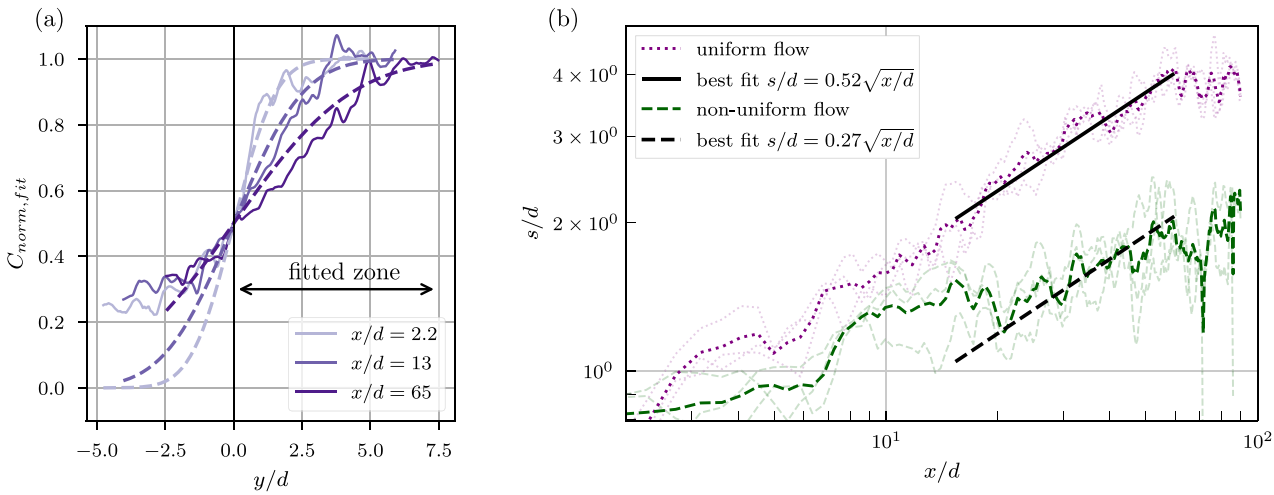

Figure 3. Mixing in porous media (packed FEP). (a) Procedure to obtain the mixing width by the fit of an error function on the upper part of the mixing interface (uniform flow, Pe = 357). The arrow indicates the fitted zone. (b) Average growth of the mixing width with distance in uniform (purple line) at Pe = 5,800 and non-uniform flow (green line) at Pe = 2,320. The average is taken over three experiments with different grain packing. The light colored lines are the three replicates for each flow, and the thick colored lines are their average. Best fits were estimated using a square root function ($s/d = A\sqrt{x/d}$) using the average mixing width of both flow cases for $15 < x/d < 60$.

The same characteristic length (L_c = 10 cm) was used for the calculation of Péclet numbers such that $U = \gamma L_c$. The 9 flow rates resulted in Péclet numbers ranging from 360 to 7,150 and 930 to 18,620 for the uniform and non-uniform flow cells respectively.

The mixing width was estimated by fitting an error function Equation 8 across the mixing interface at each distance (x/d). Because of residual light scattering by the FEP grains, the tracer concentration of the mixing front does not reach 0 in the side of the pure solution. Thus, the error function is fitted on a single side of the front, for which tracer concentrations are above 0.5 (Figure 3a). For experiments with porous media, we triplicated each experiment by repacking the FEP grains to obtain results independent of specific grain arrangements. This lead to reproducible results (Figure 3b), allowing us to capture the effect of flow non-uniformity on the evolution of the mixing scale.

3.3. Experimental Results

Figure 2c shows the experimental images obtained in the uniform and non-uniform flow cells with and without porous media. In the absence of porous media and in uniform flows (Figure 4a), the transverse mixing interface follows the classical diffusive scaling $\sqrt{x}$ (Table 1). In contrast, when imposing non-uniform flows with constant compression (Figure 4b), the mixing width becomes constant along the interface. This highlights the balance between compression and diffusion, leading to the Batchelor scale (Equation 13, table 1). Note that the sudden increase observed for $x > 5$ cm is caused by the finite size of the non-uniform flow cell, which induces a decrease of the compression rate at the outlet boundaries, and an increase of the mixing width.

In the presence of porous media, the mixing front dynamics are different as the mixing scale increases as $\sqrt{x/d}$ for both uniform and non-uniform flows (Figure 3b). This is consistent with theoretical predictions (Table 1). The non-uniform flow slightly depart from this tendency for $x < 15$d and $x > 60$d range. Indeed, close to the stagnation point, $x < 15$d, the asymptotic theory (Equation 22) is not valid anymore. Close to the outlet, the mixing width starts to interact with the boundary of the cell and fluid compression is not constant anymore, thus slowing down the observed growth. This limitation is also observed in the absence of porous media (see Figure 4b). We thus limit the quantification to the range $15 < x/d < 60$. The estimated prefactor is 0.52 for uniform flow, corresponding to a transverse dispersivity of $\alpha_T = (0.52^2/4)\, d = 0.07$ d $\pm$ 0.01 d. For non-uniform flow, the pre-factor is 0.27, which is $\sqrt{3.7}$ times smaller than for the uniform flow, close to the predicted ratio of $\sqrt{3}$ (Equation 22). This confirms that fluid compression sharpens mixing fronts in porous media, hence enhancing mixing rates.

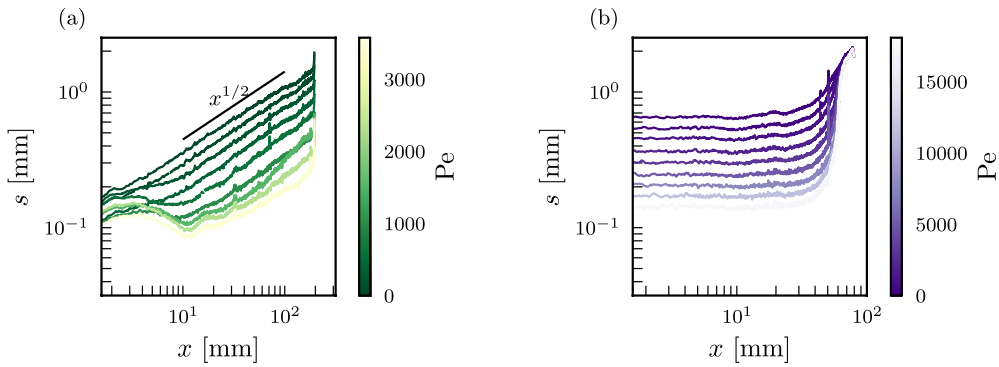

Figure 4. Mixing in Hele-Shaw diffusive cells without porous media in uniform versus non-uniform flows. (a) Mixing width as a function of x/U_x in the uniform flow configuration. (b) Mixing width as a function of x in the non-uniform flow configuration. Lines get darker when the Hele-Shaw Péclet number decreases.

In Figure 5, we plot the dependence of the mixing width with flow rate through Peclet numbers for the diffusive problem at a given position along the front. In the presence of porous media, the mixing width is independent of flow rate for both uniform and non-uniform flows. In contrast, in the absence of porous media, the mixing width decreases as $\mathrm{Pe}^{-1/2}$ in uniform and non-uniform flow. These results are in agreement with the theoretical predictions (Table 1). They highlight the properties of the Batchelor scale, as a result of the balance between compression and diffusion, and its break down under dispersion at Darcy scale. The mixing scale is still systematically smaller under fluid compression and dispersion, leading to enhanced mixing rates (Table 1).

4. Discussion and Conclusion

We investigated the effect of local dispersion versus diffusion on the properties of mixing fronts developing in uniform and non-uniform flow. For the latter, we focused on flow topologies formed around a stagnation point in converging flows, a configuration that is common for mixing fronts in hydrological and hydrogeological systems. We derived analytical solutions for the mixing width, concentration gradient and mixing rate for

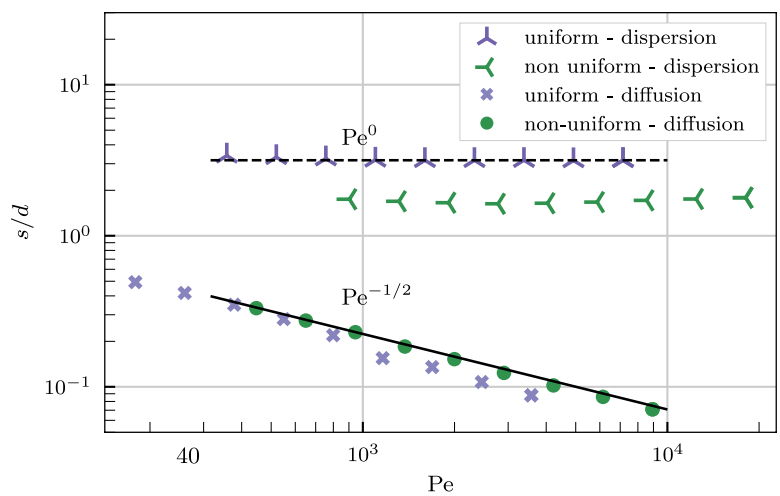

Figure 5. Mixing width as a function of flow rate through the Péclet number for diffusion and dispersion. The mixing widths in uniform and non-uniform flows in porous media (with dispersion) and in uniform diffusive Hele-Shaw flows are plotted at 40d (8 cm). For non-uniform diffusion, mixing width is averaged between the stagnation point and 10d (2 cm) (see Figure 4).

uniform and non-uniform flows and both diffusion and dispersion. We performed millifluidic tracer experiments in two parallel flat plates cells with and without porous media, showing good agreement with the theory. The results in the absence of porous media are representative of steady mixing fronts at pore scale, in a fracture or in open low Reynolds number flows. They show that fluid compression leads to the development of a fixed mixing scale independent of position but function of the flow rate for non-uniform diffusive as shown in Figure 4, hence highlighting the properties of the Batchelor scale in Equation 13. The results obtained with porous media are representative of Darcy scale mixing fronts.

In this scenario, the mixing scale increases as one moves along the mixing interface, while remaining unaffected by variations in velocity, whether in the context of uniform or non-uniform flows. Fluid compression sharpens mixing fronts by enhancing concentration gradients by a factor $\sqrt{3}$. This leads to enhanced mixing, as known from theories considering diffusion and compression, but the scaling with distance and flow rate deviates from these classical diffusive predictions.

These findings thus highlight the importance of considering dispersion or diffusion when studying mixing fronts in heterogeneous flows. The constant compression rate obtained locally in the considered non-uniform flow is analogous to chaotic flows, where a constant compression rate is sustained globally by repeated stretching and folding. This phenomenon is known to occur naturally at pores scale (Heyman et al., 2020; Lester et al., 2013, 2016; Souzy et al., 2020) and can be created by engineered pumping and injection (Fernàndez-Garcia & Rodríguez-Escales, 2023; Mays & Neupauer, 2012; Neupauer et al., 2014; Trefry et al., 2012). The obtained scaling laws (Table 1) and impact of diffusion/dispersion are thus expected to be relevant for such chaotic flows. An interesting perspective of this study is to investigate the impact of local dispersion on reaction rates in mixing fronts.

Appendix A: Mixing Width and Flux Validation With Simulations

The 2D advection-dispersion Equation 1 is numerically solved using the software OpenFoam. Figure 1 in the main text provides examples of the computed concentration fields for uniform and non-uniform flows for diffusive and dispersive, where we highlighted the mixing zone by visualizing c. For the validation with the simulations, we compute the product $c(1-c)$ across the mixing interface, which follows Equation 8:

$$c(1-c) = 1/4\left[1 - \mathrm{erf}\left(\frac{y}{s}\right)\right]^2 \tag{A1}$$

with $s = 2\sqrt{\alpha_T x}$ for uniform flow and $s = 2\sqrt{\alpha_T x/3}$ for non-uniform flow. Following (De Vriendt et al., 2022), the width of the mixing zone is taken as the distance at half the maximum of $c(1-c)$. The growth of mixing width with distance is in Figure A1, together with theoretical predictions.

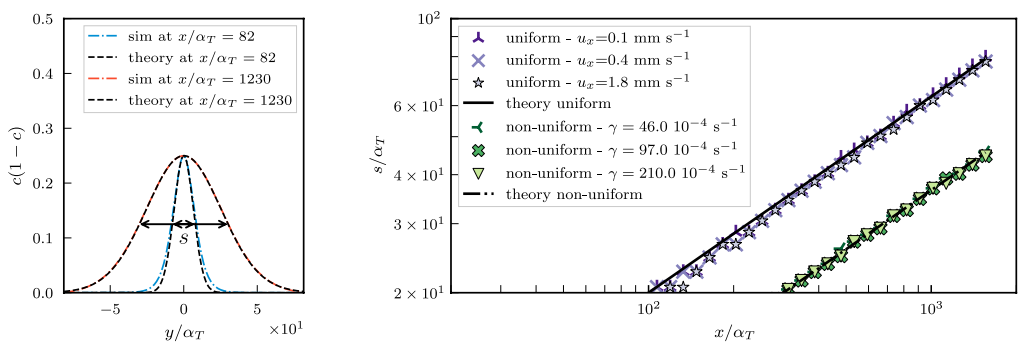

Figure A1. Simulation and theory results of the porous media (dispersive) cases in uniform and non-uniform flows. Left: Simulated against predicted $c(1-c)$ profile for the non-uniform flow case taken at two distances from the injection. Right: normalized mixing interface width from simulation at different flow conditions against the theoretical s/α_T expression as given in Equations 9 and 22.

In Figure A2, we also provide a comparison between the simulated flux calculated at the mixing front (i.e., at $y = 0$ where the flux is maximum) and the theoretical predictions. According to the theoretical devel-

opment summarized in table 1, we have $J/u(x, y = 0) = J/U = \sqrt{\alpha_T/(4\pi x)}$ for uniform flow and $J/(u(x, y = 0)) = J/(\gamma x) \sim \sqrt{3\alpha_T/(4\pi x)}$ for non-uniform flow. For both the mixing width and flux, the theoretical development is consistent with the numerical results for x. The openFoam C++/python codes for running the simulations and plotting validation figures are available in the online repository Zenodo (Rousseau et al., 2023).

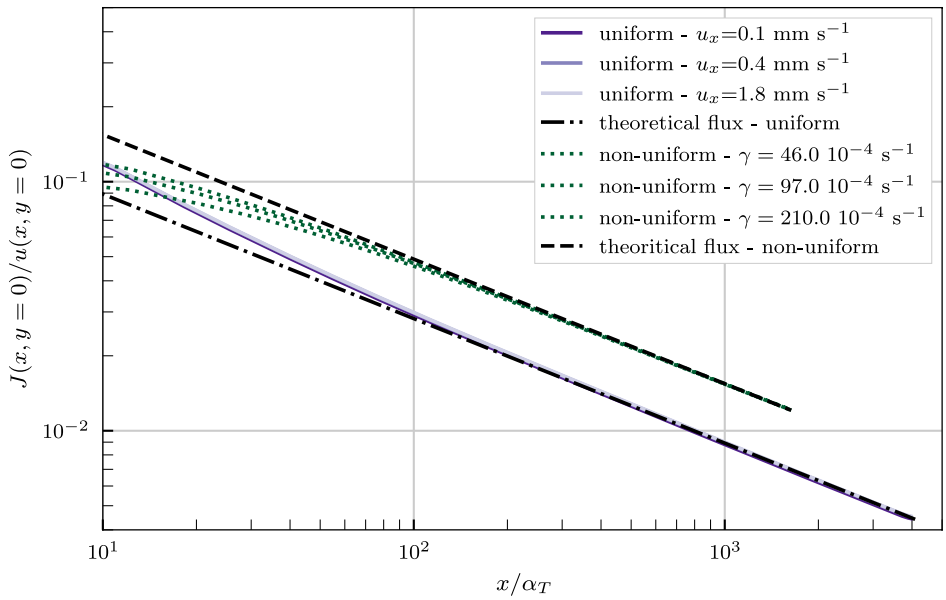

Figure A2. Normalized flux as a function of x at the mixing front interface width at $y = 0$ is plotted based on simulations at different flow conditions against the theoretical J expression as provided in Equations 11 and 24. Note that $u(x, y = 0) = U$ for uniform conditions and $u(x, y = 0) = \gamma x$ for non-uniform conditions.

Appendix B: Transparency of Fluorinated Ethylene Propylene (FEP) Grains

The Fluorinated Ethylene Propylene (FEP 100 X, Chemours©) is a translucid plastic which has the advantage to have a index of refraction (1.34) close to water (1.33). Since the FEP grains are not totally transparent for blue and green wavelengths (Figure B1a), we investigated how much each depth contributes to the image intensity. We investigate (a) how far the blue excitation wavelengths penetrate into the media and (b) how much green light reemitted by the fluorescein reached the camera (Figure B1b). To obtain these, we measured (a) the transparency of FEP to the blue backlight, (b) the transparency of FEP to the green light emitted from fluorescein, and (c) the transparency of fluorescein sodium salt solution to blue backlight. For (a) and (b), we placed different depth of the packed FEP (0, 2, 4, 6, 8, 12 mm) above the backlight (or above the illuminated fluorescein). The image intensities (normalized by the image intensity of 0 mm FEP depth) can be obtained as a function of FEP depth as $I_{F,b}(x_i)$ and $I_{F,f}(x_i)$ for packed FEP above the backlight and illuminated fluorescein, respectively, where x_i is the depth of the FEP ($x_1 = 0$ mm and $x_6 = 12$ mm). For 3), we placed different depth of fluorescein sodium salt solutions (0, 2, 4, 6, 8, 12 mm) above the backlight, which gave the normalized image intensity $I_{f,b}(x_i)$, where x_i is the depth of the fluorescein sodium salt solution ($x_1 = 0$ mm and $x_6 = 12$ mm). The backlight reaches at certain depth ($I_b(x_j)$) can be calculated by considering the transparency of FEP and fluorescein solution to the backlight, and the porosity of the packed FEP $\phi = 0.373$ as:

$$I_b(x_j) = I_b(x_{j-1}) + (I_{F,b}(x_j) - I_{F,b}(x_{j-1})) + \phi \times (I_{f,b}(x_j) - I_{f,b}(x_{j-1})) \quad \text{(B1)}$$

where x_1 corresponds to the bottom (0 mm depth) and we set $I_b(x_1)$ as 1. The decrease of the light intensity emitted by the fluorescein as a function of FEP depth is $I_{F,f}(x_i)$. Therefore, the contribution to the image intensity from a certain depth $I_c(x_j)$ is given by multiplying the backlight reached at certain depth and the decrease of the emitted light intensity as:

$$I_c(x_j) = I_b(x_j) \times I_{F,f}(x_{7-i}) \quad \text{(B2)}$$

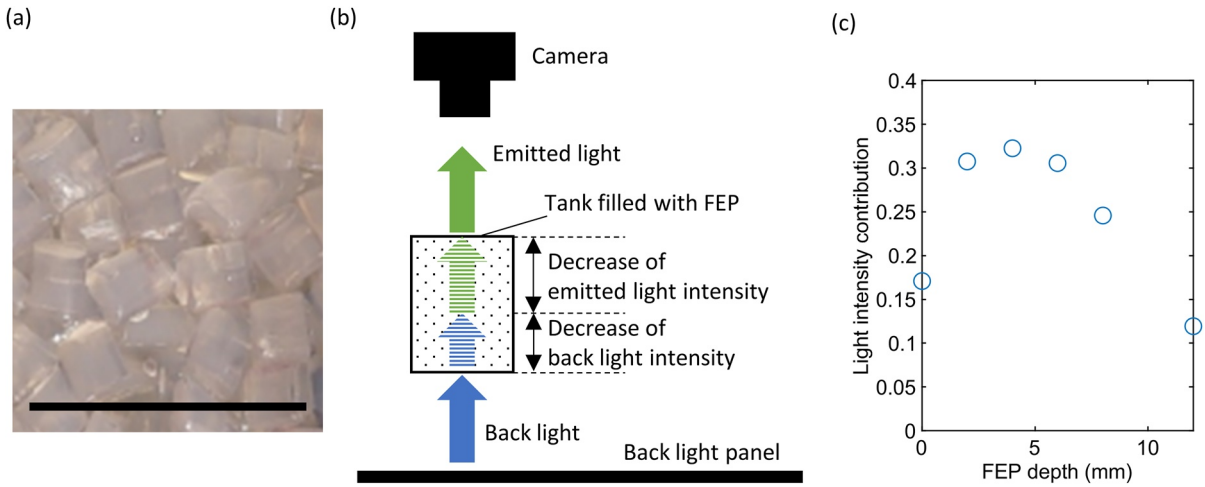

Figure B1. (a) Fluorinated Ethylene Propylene grains. The black line indicates 10 mm. (b) Schematic illustration of the emission of the light from fluorescein solution at a certain depth in a semi-transparent media. (c) Normalized received light intensity as a function of FEP packing thickness.

The results show that the I_c takes maximum at certain depth (Figrue B1c). Nevertheless, maximum I_c and minimum I_c differs only by a factor two, which suggests that the image captured the mixing in entire depth even though the FEP grains are not perfectly transparent.

Appendix C: Concentration and Light Intensity

Figure C1 shows the example of the relationship between the concentration of the fluorescein sodium salt and the image intensity at the saddle flow cell packed with FEP grains (average in 282×282 pixels). The result shows the linear relationship between the normalized concentration of the fluorescein sodium salt $C_{\text{norm},calib} = (C - C_{\text{min}})/(C_{\text{max}} - C_{\text{min}})$, where C_{min} is 0 g/L, and C_{max} is 12.5 mg/L of the fluorescein sodium salt, and the normalized intensity of the emitted light (received light) $I_{emit} = (I - I_{\text{min}})/(I_{\text{max}} - I_{\text{min}})$, where I is the image intensity, I_{min} is the image intensity at 0 g/L, and I_{max} is the image intensity at 12.5 g/L the of fluorescein sodium salt.

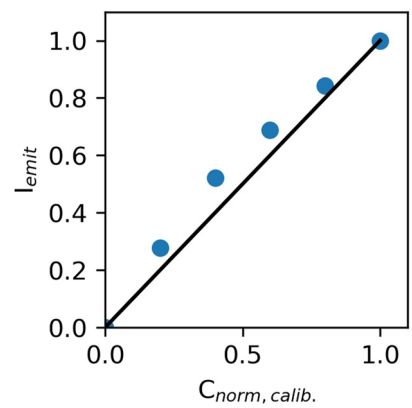

Figure C1. Normalized emitted light intensity as a function of normalized concentration.

Data Availability Statement

All experimental images and the OpenFoam solver are available on the online repository Zenodo (Rousseau et al., 2023).

Acknowledgments
J.H. and G.R. acknowledge the Grant ANR-19-CE01-0013. J.H. acknowledges the ERC Grant 101042466. We thank E. Villermaux for fruitful discussions in the fifth summer school on Flow and Transport in Porous and Fractured Media at IESC, Cargèse. We are grateful to the anonymous reviewers for the numerous astute remarks that helped to improve the paper.

References

Abarca, E., Carrera, J., Sánchez-Vila, X., & Dentz, M. (2007). Anisotropic dispersive henry problem. *Advances in Water Resources*, *30*(4), 913–926. https://doi.org/10.1016/j.advwatres.2006.08.005

Amini, N., & Hassan, Y. A. (2012). An investigation of matched index of refraction technique and its application in optical measurements of fluid flow. *Experiments in Fluids*, *53*(6), 2011–2020. https://doi.org/10.1007/s00348-012-1398-x

Bandopadhyay, A., Davy, P., & Le Borgne, T. (2018). Shear flows accelerate mixing dynamics in hyporheic zones and hillslopes. *Geophysical Research Letters*, *45*(21), 659–711. https://doi.org/10.1029/2018GL079914

Batchelor, G. K., Howells, I. D., & Townsend, A. A. (1959). Small-scale variation of convected quantities like temperature in turbulent fluid Part 2. The case of large conductivity. *Journal of Fluid Mechanics*, *5*(01), 134. https://doi.org/10.1017/S0022112059000106

Bear, J. (1988). *Dynamics of fluids in porous media*. Dover Publications.

Bochet, O., Bethencourt, L., Dufresne, A., Farasin, J., Pédrot, M., Labasque, T., et al. (2020). Iron-oxidizer hotspots formed by intermittent oxic–anoxic fluid mixing in fractured rocks. *Nature Geoscience*, *13*(2), 149–155. https://doi.org/10.1038/s41561-019-0509-1

Bouchez, J., Lajeunesse, E., Gaillardet, J., France-Lanord, C., Dutra-Maia, P., & Maurice, L. (2010). Turbulent mixing in the amazon river: The isotopic memory of confluences. *Earth and Planetary Science Letters*, *290*(1–2), 37–43. https://doi.org/10.1016/j.epsl.2009.11.054

Bresciani, E., Kang, P. K., & Lee, S. (2019). Theoretical analysis of groundwater flow patterns near stagnation points. *Water Resources Research*, *55*(2), 1624–1650. https://doi.org/10.1029/2018WR023508

Burté, L., Cravotta, C., Bethencourt, L., Farasin, J., Pédrot, M., Dufresne, A., et al. (2019). Kinetic study on clogging of a geothermal pumping well triggered by mixing-induced biogeochemical reactions. *Environmental Science and Technology*, *53*(10), 5848–5857. https://doi.org/10.1021/acs.est.9b00453

Casalini, T., Salvalaglio, M., Perale, G., Masi, M., & Cavallotti, C. (2011). Diffusion and aggregation of sodium fluorescein in aqueous solutions. *Journal of Physical Chemistry B*, *115*(44), 12896–12904. https://doi.org/10.1021/jp207459k

Chiogna, G., Hochstetler, D. L., Bellin, A., Kitanidis, P. K., & Rolle, M. (2012). Mixing, entropy and reactive solute transport. *Geophysical Research Letters*, *39*(20), L20405. https://doi.org/10.1029/2012gl053295

Cirpka, O. A., Chiogna, G., Rolle, M., & Bellin, A. (2015). Transverse mixing in three-dimensional nonstationary anisotropic heterogeneous porous media. *Water Resources Research*, *51*(1), 241–260. https://doi.org/10.1002/2014wr015331

Cirpka, O. A., de Barros, F. P., Chiogna, G., Rolle, M., & Nowak, W. (2011). Stochastic flux-related analysis of transverse mixing in two-dimensional heterogeneous porous media. *Water Resources Research*, *47*(6), W06515. https://doi.org/10.1029/2010wr010279

De Barros, F. P., Dentz, M., Koch, J., & Nowak, W. (2012). Flow topology and scalar mixing in spatially heterogeneous flow fields. *Geophysical Research Letters*, *39*(8), L08404. https://doi.org/10.1029/2012gl051302

Delgado, J. M. (2007). Longitudinal and transverse dispersion in porous media. *Chemical Engineering Research and Design*, *85*(9A), 1245–1252. https://doi.org/10.1205/cherd07017

Dentz, M., Hidalgo, J. J., & Lester, D. (2023). Mixing in porous media: Concepts and approaches across scales. *Transport in Porous Media*, *146*(1–2), 5–53. https://doi.org/10.1007/s11242-022-01852-x

Dentz, M., Le Borgne, T., Englert, A., & Bijeljic, B. (2011). Mixing, spreading and reaction in heterogeneous media: A brief review. *Journal of Contaminant Hydrology*, *120–121*(C), 1–17. https://doi.org/10.1016/j.jconhyd.2010.05.002

De Vriendt, K. (2021). *Mixing and chemical reaction hotspots in saline-freshwater mixing zones (PhD thesis)*. Universitat Politècnica de Catalunya. Departament d'Enginyeria Civil i Ambiental. https://doi.org/10.5821/dissertation-2117-351092

De Vriendt, K., Le Borgne, T., Pool, M., & Dentz, M. (2022). Subsurface mixing dynamics across the salt-freshwater interface. *Geophysical Research Letters*, *49*(7), e2021GL097094. https://doi.org/10.1029/2021gl097094

De Wit, A. (2020). Chemo-hydrodynamic patterns and instabilities. *Annual Review of Fluid Mechanics*, *52*(1), 531–555. https://doi.org/10.1146/annurev-fluid-010719-060349

Engdahl, N. B., Benson, D. A., & Bolster, D. (2014). Predicting the enhancement of mixing-driven reactions in nonuniform flows using measures of flow topology. *Physical Review E*, *90*(5), 051001. https://doi.org/10.1103/physreve.90.051001

Fernàndez-Garcia, D., & Rodríguez-Escales, P. (2023). Enhancing mixing during groundwater remediation via engineered injection-extraction: The issue of connectivity. *Water Resources Research*, *59*, e2023WR034934. https://doi.org/10.1029/2023WR034934

Fu, F., Dionysiou, D. D., & Liu, H. (2014). The use of zero-valent iron for groundwater remediation and wastewater treatment: A review. *Journal of Hazardous Materials*, *267*, 194–205. https://doi.org/10.1016/j.jhazmat.2013.12.062

Hester, E. T., Cardenas, M. B., Haggerty, R., & Apte, S. V. (2017). The importance and challenge of hyporheic mixing. *Water Resources Research*, *53*(5), 3565–3575. https://doi.org/10.1002/2016WR020005

Heyman, J., Lester, D. R., Turuban, R., Méheust, Y., & Le Borgne, T. (2020). Stretching and folding sustain microscale chemical gradients in porous media. *Proceedings of the National Academy of Sciences of the United States of America*, *117*(24), 13359–13365. https://doi.org/10.1073/pnas.2002858117

Hidalgo, J. J., Dentz, M., Cabeza, Y., & Carrera, J. (2015). Dissolution patterns and mixing dynamics in unstable reactive flow. *Geophysical Research Letters*, *42*(15), 6357–6364. https://doi.org/10.1002/2015GL065036

Izumoto, S., Huisman, J. A., Zimmermann, E., Heyman, J., Gomez, F., Tabuteau, H., et al. (2022). Pore-scale mechanisms for spectral induced polarization of calcite precipitation inferred from geo-electrical millifluidics. *Environmental Science & Technology*, *56*(8), 4998–5008. https://doi.org/10.1021/acs.est.1c07742

Karadimitriou, N. K., & Hassanizadeh, S. M. (2012). A review of micromodels and their use in two-phase flow studies. *Vadose Zone Journal*, *11*(3), vzj2011.0072. https://doi.org/10.2136/vzj2011.0072

Le Borgne, T., Dentz, M., & Villermaux, E. (2013). Stretching, coalescence, and mixing in porous media. *Physical Review Letters*, *110*(20), 1–5. https://doi.org/10.1103/PhysRevLett.110.204501

Le Borgne, T., Dentz, M., & Villermaux, E. (2015). The lamellar description of mixing in porous media. *Journal of Fluid Mechanics*, *770*, 458–498. https://doi.org/10.1017/jfm.2015.117

Le Borgne, T., Ginn, T. R., & Dentz, M. (2014). Impact of fluid deformation on mixing-induced chemical reactions in heterogeneous flows. *Geophysical Research Letters*, *41*(22), 7898–7906. https://doi.org/10.1002/2014GL062038

Lester, D. R., Metcalfe, G., & Trefry, M. G. (2013). Is chaotic advection inherent to porous media flow? *Physical Review Letters*, *111*(17), 174101. https://doi.org/10.1103/PhysRevLett.111.174101

Lester, D. R., Trefry, M. G., & Metcalfe, G. (2016). Chaotic advection at the pore scale: Mechanisms, upscaling and implications for macroscopic transport. *Advances in Water Resources*, *97*, 175–192. https://doi.org/10.1016/j.advwatres.2016.09.007

Lysyy, M., Føyen, T., Johannesen, E. B., Fernø, M., & Ersland, G. (2022). Hydrogen relative permeability hysteresis in underground storage. *Geophysical Research Letters*, *49*(17), e2022GL100364. https://doi.org/10.1029/2022GL100364

Mays, D. C., & Neupauer, R. M. (2012). Plume spreading in groundwater by stretching and folding. *Water Resources Research*, *48*(7), W07501. https://doi.org/10.1029/2011wr011567

Neupauer, R. M., Meiss, J. D., & Mays, D. C. (2014). Chaotic advection and reaction during engineered injection and extraction in heterogeneous porous media. *Water Resources Research*, *50*(2), 1433–1447. https://doi.org/10.1002/2013wr014057

Perez, L. J., Hidalgo, J. J., & Dentz, M. (2019). Upscaling of mixing-limited bimolecular chemical reactions in Poiseuille flow. *Water Resources Research*, *55*(1), 249–269. https://doi.org/10.1029/2018wr022730

Prandle, D. (2009). *Estuaries: Dynamics, mixing, sedimentation and morphology*. Cambridge University Press.

Rolle, M., Eberhardt, C., Chiogna, G., Cirpka, O. A., & Grathwohl, P. (2009). Enhancement of dilution and transverse reactive mixing in porous media: Experiments and model-based interpretation. *Journal of Contaminant Hydrology*, *110*(3–4), 130–142. https://doi.org/10.1016/j.jconhyd.2009.10.003

Rolle, M., & Le Borgne, T. (2019). Mixing and reactive fronts in the subsurface. *Reviews in Mineralogy and Geochemistry*, *85*(1), 111–142. https://doi.org/10.2138/rmg.2018.85.5

Rousseau, G., Izumoto, S., Le Borgne, T., & Heyman, J. (2023). Solute dispersion in accelerating flows [Dataset]. Zenodo. https://doi.org/10.5281/zenodo.8384168

Souzy, M., Lhuissier, H., Méheust, Y., Le Borgne, T., & Metzger, B. (2020). Velocity distributions, dispersion and stretching in three-dimensional porous media. *Journal of Fluid Mechanics*, *891*, A16. https://doi.org/10.1017/jfm.2020.113

Szulczewski, M. L., MacMinn, C. W., Herzog, H. J., & Juanes, R. (2012). Lifetime of carbon capture and storage as a climate-change mitigation technology. *Proceedings of the National Academy of Sciences of the United States of America*, *109*(14), 5185–5189. https://doi.org/10.1073/pnas.1115347109

Tarkowski, R. (2019). *Underground hydrogen storage: Characteristics and prospects* (Vol. 105). Elsevier Ltd. https://doi.org/10.1016/j.rser.2019.01.051

Trefry, M. G., Lester, D. R., Metcalfe, G., Ord, A., & Regenauer-Lieb, K. (2012). Toward enhanced subsurface intervention methods using chaotic advection. *Journal of Contaminant Hydrology*, *127*(1–4), 15–29. https://doi.org/10.1016/j.jconhyd.2011.04.006

Valocchi, A. J., Bolster, D., & Werth, C. J. (2019). Mixing-limited reactions in porous media. *Transport in Porous Media*, *130*(1), 157–182. https://doi.org/10.1007/s11242-018-1204-1

Villermaux, E. (2019). Mixing versus stirring. *Annual Review of Fluid Mechanics*, *51*(1), 245–273. https://doi.org/10.1146/annurev-fluid-010518-040306

Wang, Y., Fernàndez-Garcia, D., Sole-Mari, G., & Rodríguez-Escales, P. (2022). Enhanced NAPL removal and mixing with engineered injection and extraction. *Water Resources Research*, *58*(4), e2021WR031114. https://doi.org/10.1029/2021WR031114

Ye, Y., Chiogna, G., Cirpka, O. A., Grathwohl, P., & Rolle, M. (2015). Experimental evidence of helical flow in porous media. *Physical Review Letters*, *115*(19), 194502. https://doi.org/10.1103/physrevlett.115.194502

Ye, Y., Chiogna, G., Lu, C., & Rolle, M. (2020). Plume deformation, mixing, and reaction kinetics: An analysis of interacting helical flows in three-dimensional porous media. *Physical Review E*, *102*(1), 1–12. https://doi.org/10.1103/PhysRevE.102.013110

Yuan, S.-Y., Xu, L., Tang, H.-W., Xiao, Y., & Gualtieri, C. (2022). The dynamics of river confluences and their effects on the ecology of aquatic environment: A review. *Journal of Hydrodynamics*, *34*(1), 1–14. https://doi.org/10.1007/s42241-022-0001-z

Ziliotto, F., Basilio Hazas, M., Rolle, M., & Chiogna, G. (2021). Mixing enhancement mechanisms in aquifers affected by hydropeaking: Insights from flow-through laboratory experiments. *Geophysical Research Letters*, *48*(21), e2021GL095336. https://doi.org/10.1029/2021GL095336

Zoback, M. D., & Gorelick, S. M. (2012). Earthquake triggering and large-scale geologic storage of carbon dioxide. *Proceedings of the National Academy of Sciences*, *109*(26), 10164–10168. https://doi.org/10.1073/pnas.1202473109